

Supporting Information

Magnetic Field Enhanced Charge Conduction in Paramagnetic Nickel (II)-Cysteine Heterostructures

Manajit Mandal, Abhik Ghoshal, Ankur Malik, Prakash Chandra Mondal*

Department of Chemistry, Indian Institute of Technology Kanpur, Uttar Pradesh-208016, India

E-mail: pcmondal@iitk.ac.in (P.C.M.)

Content

| | |
|--|------------|
| 1. Instrumentations..... | S3 |
| 2. FT-IR spectra | S4 |
| 3. XRD pattern of L/D-Cys-Ni (II) heterostructures..... | S4 |
| 4. XPS data of L/D-Cys-Ni (II) heterostructures and Ni(OH)₂..... | S5 |
| 5. Morphology analysis..... | S7 |
| 6. Hydrodynamic size analysis using DLS studies..... | S8 |
| 7. Thermogravimetric-differential thermal analysis (TG-DTA)..... | S9 |
| 8. Calculation of Ni:L/D-Cys compositions from TG-DTA curves..... | S9 |
| 9. Vibrating-sample magnetometer (VSM) measurement setup | S10 |
| 10. M-H hysteresis loops | S10 |
| 11. UV-vis spectra | S11 |
| 12. CD spectra..... | S11 |
| 13. Calculation of dissymmetry g-factor value..... | S11 |
| 14. Optical microscopy image and current-voltage measurements | S12 |
| 15. Schematic diagram and current-voltage behavior of the electrical devices | S13 |
| 16. Current density-voltage (j-V) characteristics with configuration Ni/Gel/ITO..... | S14 |
| 17. Optical microscopy images..... | S14 |
| 18. Study of film morphology without and with magnetic field..... | S15 |
| 19. Current density-voltage (j-V) characteristics | S16 |
| 20. Solid-state device's electrical parameter..... | S18 |
| 21. Control studies for magneto-electrochemical measurements..... | S19 |
| 22. Statistical data of magneto-electrochemistry measurements..... | S20 |
| 23. Magneto-electrochemistry of achiral Ni(II) heterostructures, and Ni(OH)₂ | S21 |
| 24. Chronoamperometry measurements for Chiral L/D-Cys-Ni (II)..... | S21 |
| 25. Electrochemical parameters deduced from the equivalent model circuit..... | S21 |
| 26. References..... | S22 |

1. Instrumentations

Fourier-transform infrared (FT-IR) spectra were measured on a Bruker Optik GmbH Alpha II spectrophotometer. The spectra were collected in KBr pallet mode within a frequency range of 4000 - 400 cm^{-1} by accumulating 32 scans. The final spectra were plotted after baseline correction and subtracting water vapor and carbon dioxide stretching mode using the OPUS 8.1 software. X-ray photoelectron spectra (XPS) were performed on PHI 5000 Versa Probe II FEI Inc. using Al $\text{K}\alpha$ as the radiation source. All the recorded XPS spectra were calibrated using C 1s peak (BE = 284.8 eV), and all the data were analyzed and plotted using Origin software. The X-ray diffraction (XRD) spectra were recorded on X-ray diffractometer (Malvern PANalytical's X'Pert³ MRD) with Cu $\text{K}\alpha$ ($\lambda = 0.15405 \text{ nm}$) radiation source and scanning speed of 2° min^{-1} (operated at 40 kV and 40 mA). PXRD data was analyzed on X'Pert HighScore Plus software database for phase identification and semi-quantitative phase analysis. A thin layer of gold was coated on the powdered samples for recording the surface morphology of heterostructures using a Field-emission scanning electron microscope (FE-SEM) (Zeiss, Model; SUPRA 40 VP) equipped with a field-emission cold cathode as an electron source and two different detectors (SE2, InLens). All the images were taken in suitable InLens mode and 3-4 mm as the working distance (WD). All the cross-sectional optical microscopy images were taken using Olympus upright microscope model BX53M and images were analysed by stream basic software. A high-resolution transmission electron microscopic (HR-TEM) study was performed by employing FEI Tecnai G2 12-TWIN electron microscope operating at an acceleration voltage of 120 kV, equipped with (lanthanum hexaboride) LaB₆ filament as an electron source. Nearly 20 μL colloidal solution was placed on a carbon-coated TEM grid, which was further dried in a desiccator. The crystalline nature of the samples was analyzed by selected area electron diffraction (SAED). The UV-vis spectra were recorded using a JASCO V-770 UV-Visible-NIR spectrophotometer (light source: 30 W Deuterium lamp, 20 W Halogen lamp) and recorded at a speed of 200 nm min^{-1} . A quartz cuvette (optical path length = 10 mm) was used to record all the spectra. Circular dichroism (CD) spectra were recorded on a CD Spectrometer (J-815) instrument (optical path length = 3 mm). All the spectra were recorded at a speed of 200 nm min^{-1} and accumulated 3 times by avoiding (High Tension) HT voltage of more than 800 V. The Dynamic Light Scattering (DLS) measurements were performed using Zetasizer Pro, operated on the principle of Non-Invasive Back Scatter (NIBS). All the measurements were taken within a quartz cuvette (both sides transparent) of a path length of 10 mm.

2. FT-IR spectra

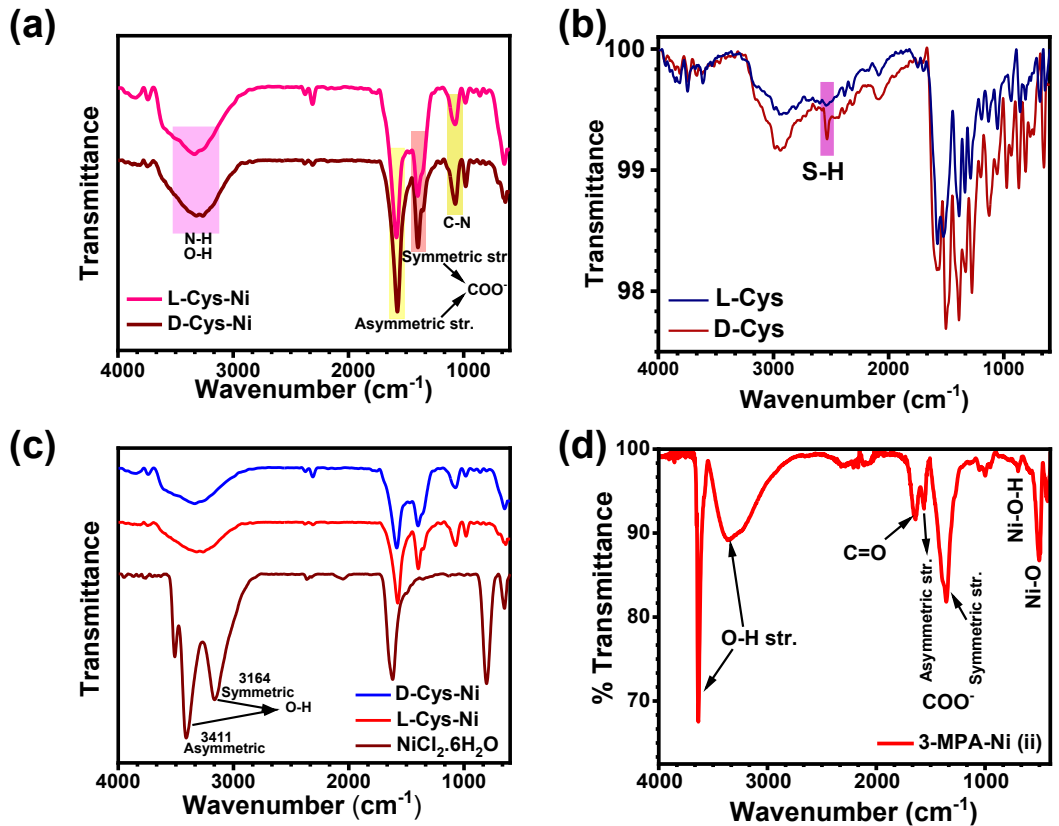


Fig S1. FT-IR spectra of (a) L/D-Cys-Ni (II) heterostructures, comparison of spectrum of (b) pure L/D-Cys, (c) L/D-Cys-Ni (II) heterostructures and metal precursor, NiCl₂.6H₂O, and (d) 3-MPA-Ni complex.

3. X-ray diffraction pattern of L/D-Cys-Ni (II) heterostructures

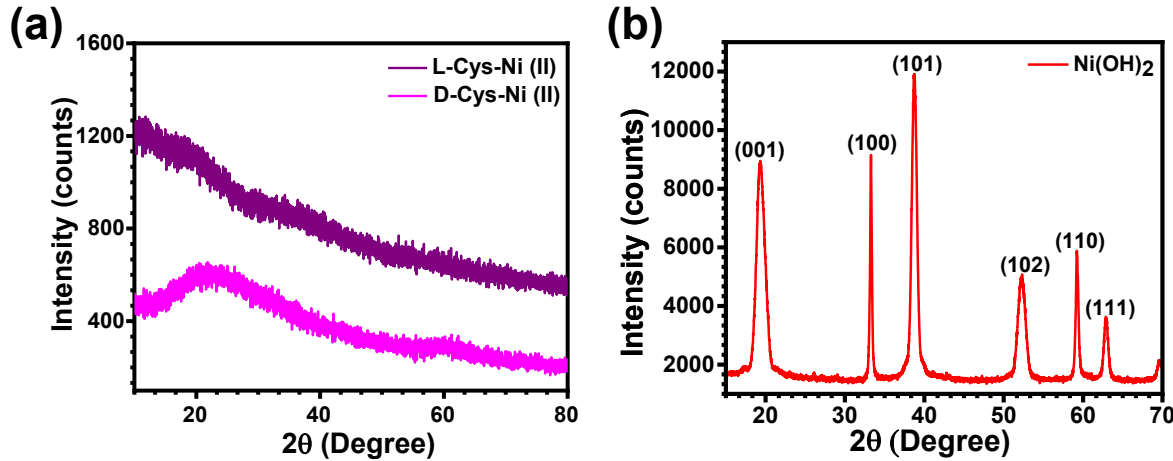


Fig S2. Comparison XRD spectrum of (a) L/D-Cys-Ni (II) heterostructures and (b) Ni(OH)₂.

4. X-ray photoelectron spectra of L/D-Cys-Ni (II) heterostructures and Ni(OH)₂

4a. Characteristic Carbon and oxygen XPS signals in L/D-Cys-Ni (II) nanostructure

The C 1s signal is deconvoluted in four peaks corresponding to C-C, C-N, C-S and O-C=O, and the O 1s signal is fitted for two peaks corresponding to C-O and C-O-H for both L/D-Cys-Ni (II) heterostructures.^{1–3}. All the binding energy values are presented in tabular form (**Table S1**).

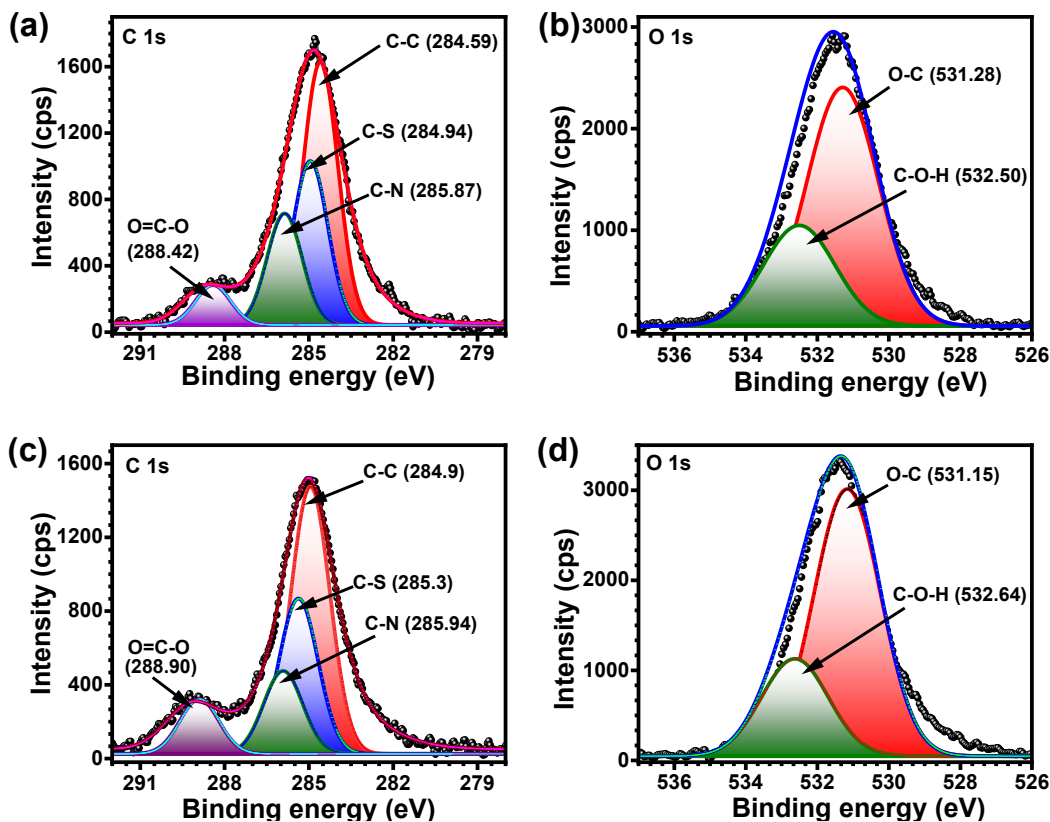


Fig S3. XPS signals of (a) C 1s, (b) O 1s of L-Cys-Ni (II), and (c) C 1s , (d) O 1s of D-Cys-Ni (II).

4b. Characteristic nickel and oxygen XPS spectra of Ni(OH)₂

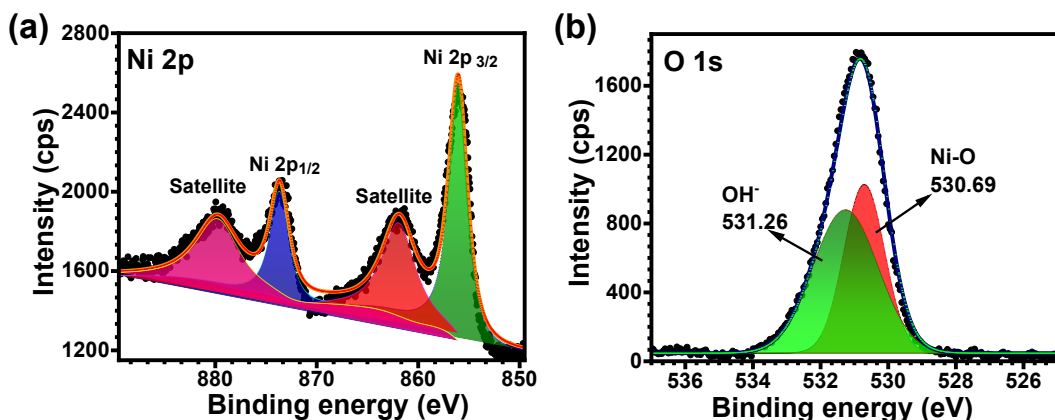


Fig S4. Characteristic XPS signals of (a) Ni 2p and (b) O 1s of Ni(OH)₂.

4c. XPS survey spectra of L/D-Cys-Ni (II) and Ni(OH)₂

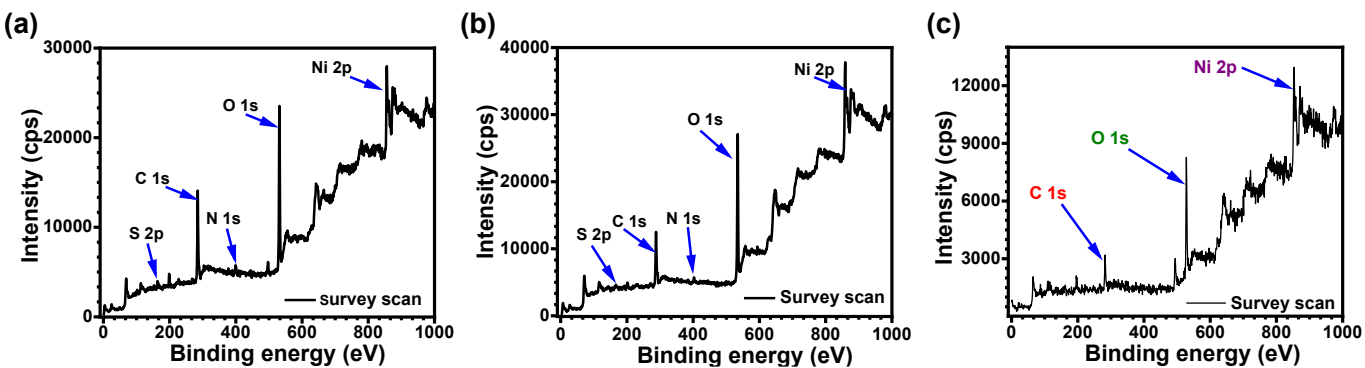


Fig S5. XPS Survey spectra of (a) L-Cys-Ni (II), (b) D-Cys-Ni (II) nanostructure, and (c) Ni(OH)₂.

Table S1. Binding energy values from the fitted XPS spectra of L-Cys-Ni (II), D-Cys-Ni(II), and Ni(OH)₂.

| Sl. No. | Compositions | Elements | Binding energy (eV) |
|---------|---------------|----------|--|
| 1. | L-Cys-Ni (II) | C 1s | 284.59 (C-C) |
| | | | 284.94 (C-S) |
| | | | 285.87 (C-N) |
| | | | 288.42 (O-C=O) |
| | | O 1s | 531.28 (O-C) |
| | | | 532.50 (C-O-H) |
| | | N 1s | 399.07 (N-C) |
| | | | 400.27 (N-Ni) |
| | | S 2p | 163.32 (2p _{1/2}) |
| | | | 161.97 (2p _{3/2}) |
| | | | 164 (C-S) |
| | | | 168.92 (Satellite peak) |
| | | Ni 2p | 879.82 (Ni ⁺² , 2p _{1/2} satellite peak) |
| | | | 873.62 (Ni ⁺² , 2p _{1/2}) |
| | | | 861.42 (Ni ⁺² , 2p _{3/2} satellite peak) |
| | | | 855.67 (Ni ⁺² , 2p _{3/2}) |
| 2. | D-Cys-Ni (II) | C 1s | 284.9 (C-C) |
| | | | 285.3 (C-S) |
| | | | 285.94 (C-N) |
| | | | 288.90 (O-C=O) |
| | | O 1s | 531.15 (O-C) |
| | | | 532.64 (C-O-H) |
| | | N 1s | 399.34 (N-C) |
| | | | 400.94 (N-Ni) |

| | | | |
|----|---------------------|---|---|
| 2. | S 2p | 162.89 ($2p_{1/2}$) | |
| | | 161.14 ($2p_{3/2}$) | |
| | | 163.9 (C-S) | |
| | | 168.09 (Satellite peak) | |
| | Ni 2p | 879.74 (Ni^{+2} , $2p_{1/2}$ satellite peak) | |
| | | 873.69 (Ni^{+2} , $2p_{1/2}$) | |
| | | 861.34 (Ni^{+2} , $2p_{3/2}$ satellite peak) | |
| | | 855.79 (Ni^{+2} , $2p_{3/2}$) | |
| 3. | Ni(OH) ₂ | O 1s | 530.69 (Ni-O) |
| | | | 531.26 (OH ⁻) |
| | | Ni 2p | 873.69 (Ni^{+2} , $2p_{1/2}$) |
| | | | 879.89 (Ni^{+2} , $2p_{1/2}$ satellite peak) |
| | | | 856.09 (Ni^{+2} , $2p_{3/2}$) |
| | | | 861.99 (Ni^{+2} , $2p_{3/2}$ satellite peak) |

5. Morphology and particles size analysis

5a. FE-SEM and TEM of L-Cys-Ni (II), D-Cys-Ni (II)

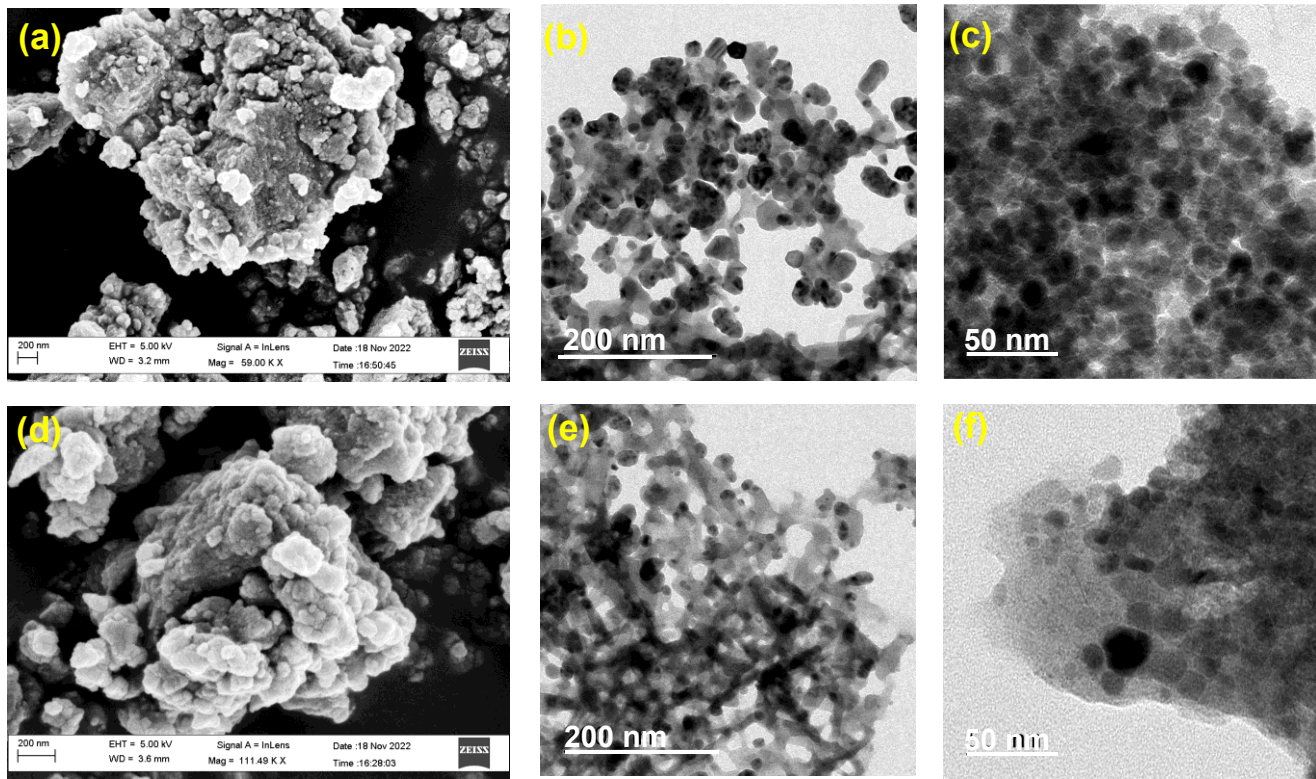


Fig S6. FE-SEM images of (a) L-Cys-Ni (II), (b-c) TEM images of L-Cys-Ni (II). FE-SEM images of (d) D-Cys-Ni (II), and (e-f) TEM images of D-Cys-Ni (II).

5b. Size distribution histogram diagram

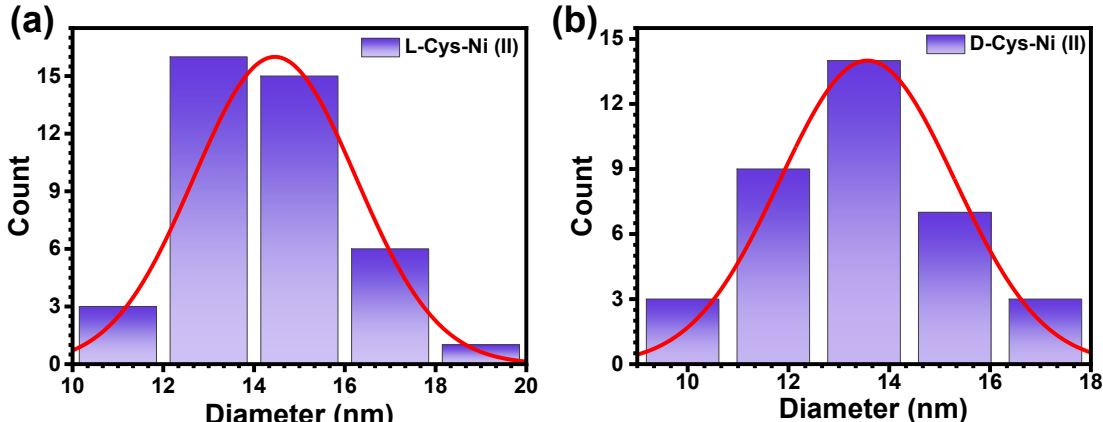


Fig S7. Calculation of particle size from size distribution histogram of (a) L-Cys-Ni (II), and (b) D-Cys-Ni (II).

Table S2. Average particle size of L-Cys-Ni (II) and D-Cys-Ni (II)

| | Sample | Particle size (nm) |
|----|---------------|--------------------|
| 1. | L-Cys-Ni (II) | 14.4 ± 1.76 |
| 2. | D-Cys-Ni (II) | 13.6 ± 1.71 |

6. Hydrodynamic size analysis using DLS studies

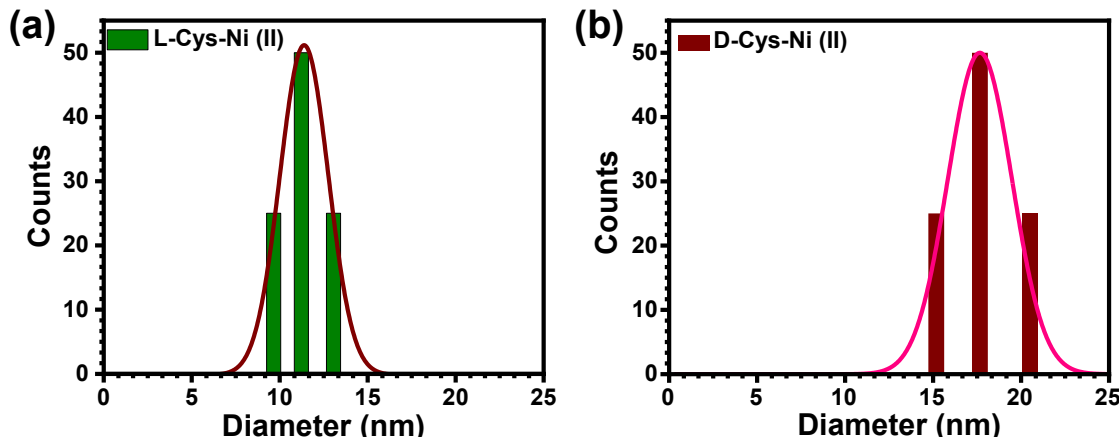


Fig S8. The hydrodynamic sizes of (a) L-Cys-Ni (II), and (b) D-Cys-Ni (II) are 11.3 ± 0.03 nm, and 17.6 ± 0.12 nm, respectively, calculated from Dynamic Light Scattering (DLS) measurement.

7. Thermogravimetric analysis (TG-DTG)

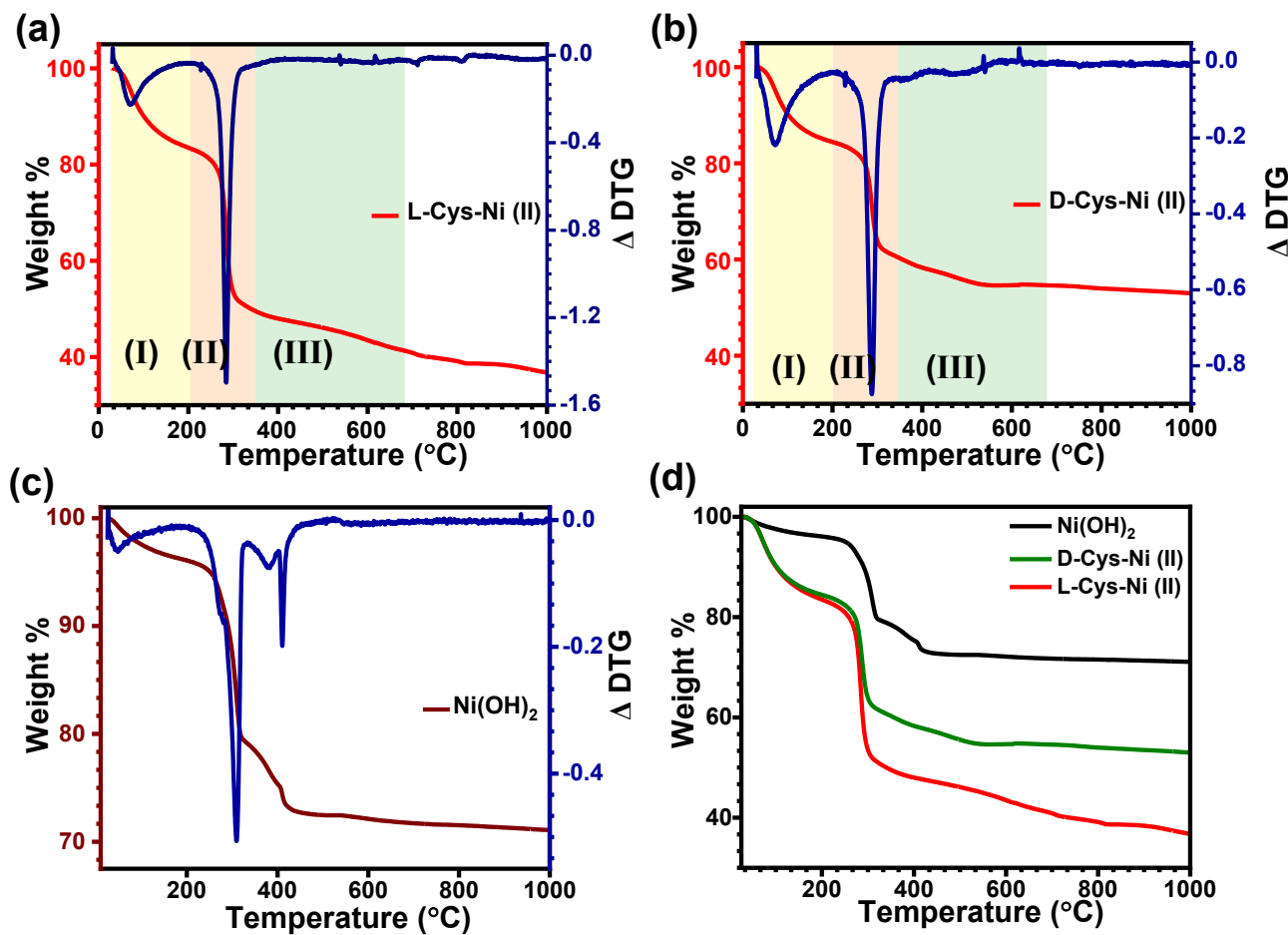


Fig S9. Thermogravimetric analysis (TG-DTG) curves and the first derivative of weight percentage for (a) L-Cys-Ni (II), and (b) D-Cys-Ni (II), (c) Ni(OH)₂ and (d) comparison TGA spectra of L-Cys-Ni (II), D-Cys-Ni (II) and Ni(OH)₂.

8. Calculation of Ni: L/D-Cys compositions from TG-DTG curves

The weight loss behavior of materials was interpreted through the following three regions of TGA curve.

(I) Desorption of physically adsorbed water.

(II) Release of water from interlayers and evaporation of organic chiral ligands with an exothermic peak and full combustion of chiral ligands.

(III) Formation of NiO.

Total weight loss in weight percentage for Ni, since NiO (74.7 g/mol) is formed after oxidation, Ni (mol) present in the sample is given by eq. (i)⁴.

$$\text{mass in gm} \times \frac{(100-(\text{I}+\text{II}+\text{III}))}{100} \times \frac{1}{74.7} = X (\mu\text{mol}) \quad \dots \dots \text{(i)}$$

The amount of Ni present in D-Cys-Ni (II) was estimated at 21.9 μmol , and the weight loss for D-Cys (organic ligands) in region (II) is 29.7 μmol . This value determines the ratio of D-Cys : Ni (II) is 1.35:1. Therefore, the chemical formula of the nanostructure is considered as $(\text{D-Cys})_{1.35}\text{-Ni (II)}$ and similarly $(\text{L-Cys})_{1.60}\text{-Ni (II)}$.

9. Vibrating-sample magnetometer (VSM) measurement setup

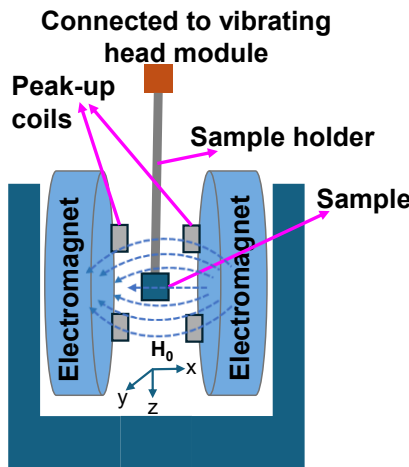


Fig S10. Scheme for the VSM measurements of magnetic heterostructures used for recording M-H hysteresis loops.

10. M-H hysteresis loops and M-T

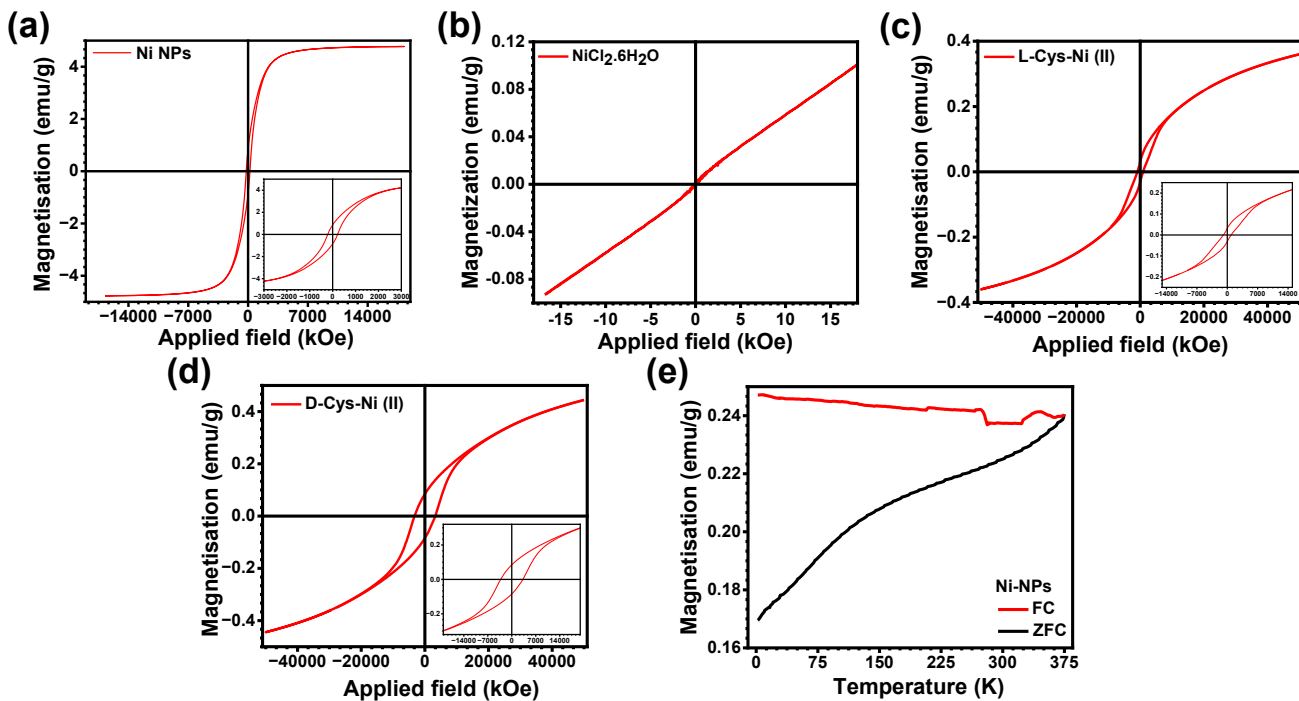


Fig S11. M-H hysteresis loop at 298 K for (a) Ni NPs, (b) pure $\text{NiCl}_2 \cdot 6\text{H}_2\text{O}$. M-H hysteresis loop at 2 K for (c) L-Cys-Ni (II), and (d) D-Cys-Ni (II), and (e) M-T of bare Ni NPs.

11. UV-vis spectra

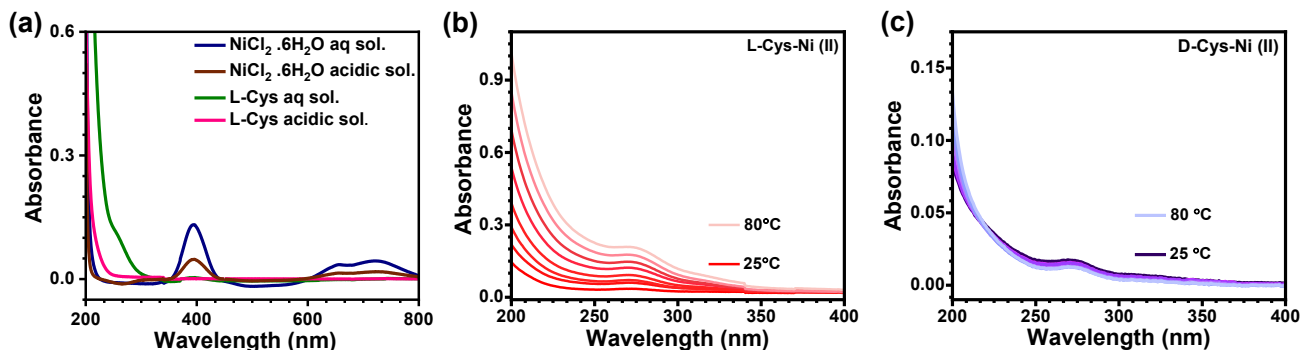


Fig S12. Optical studies of L/D-Cys-Ni (II) heterostructures. (a) UV-Vis spectra of hydrated Ni salt, L-Cys recorded in aqueous solution and aqueous acidic solution, and Temperature-dependent UV-vis spectra of chiral heterostructures (b) L-Cys-Ni (II), and (c) D-Cys-Ni (II).

12. CD spectra

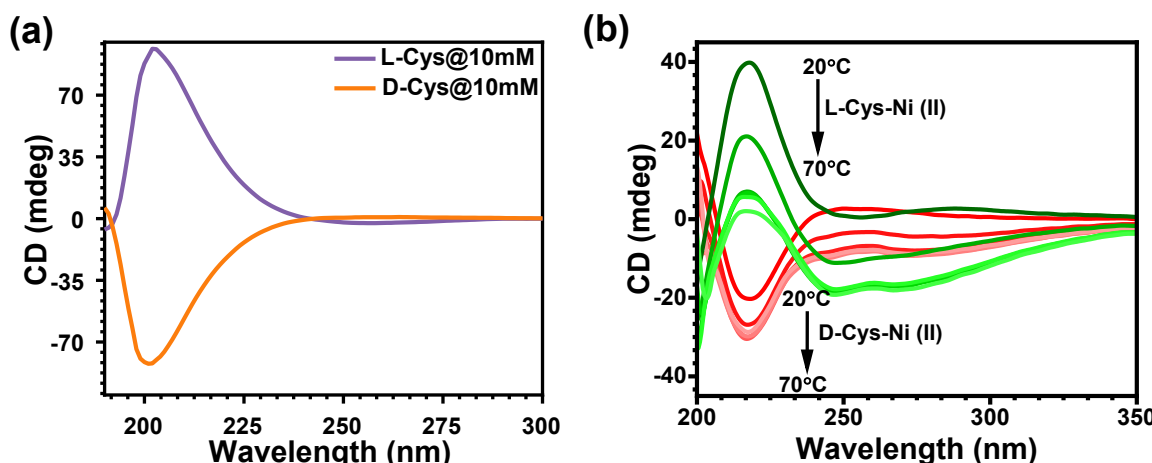


Fig S13. Chiroptical studies of L/D-Cys-Ni (II) heterostructures. (a) circular dichroism spectra of pure chiral ligands, and (b) Temperature-dependent CD spectra of chiral materials L/D-Cys-Ni (II).

13. Calculation of dissymmetry g-factor value

$$g = \frac{\text{CD (in mdeg)}}{32980 \times \text{Absorbance}} \dots \dots \dots \text{(ii)}$$

14. Optical microscopy image and current-voltage measurements

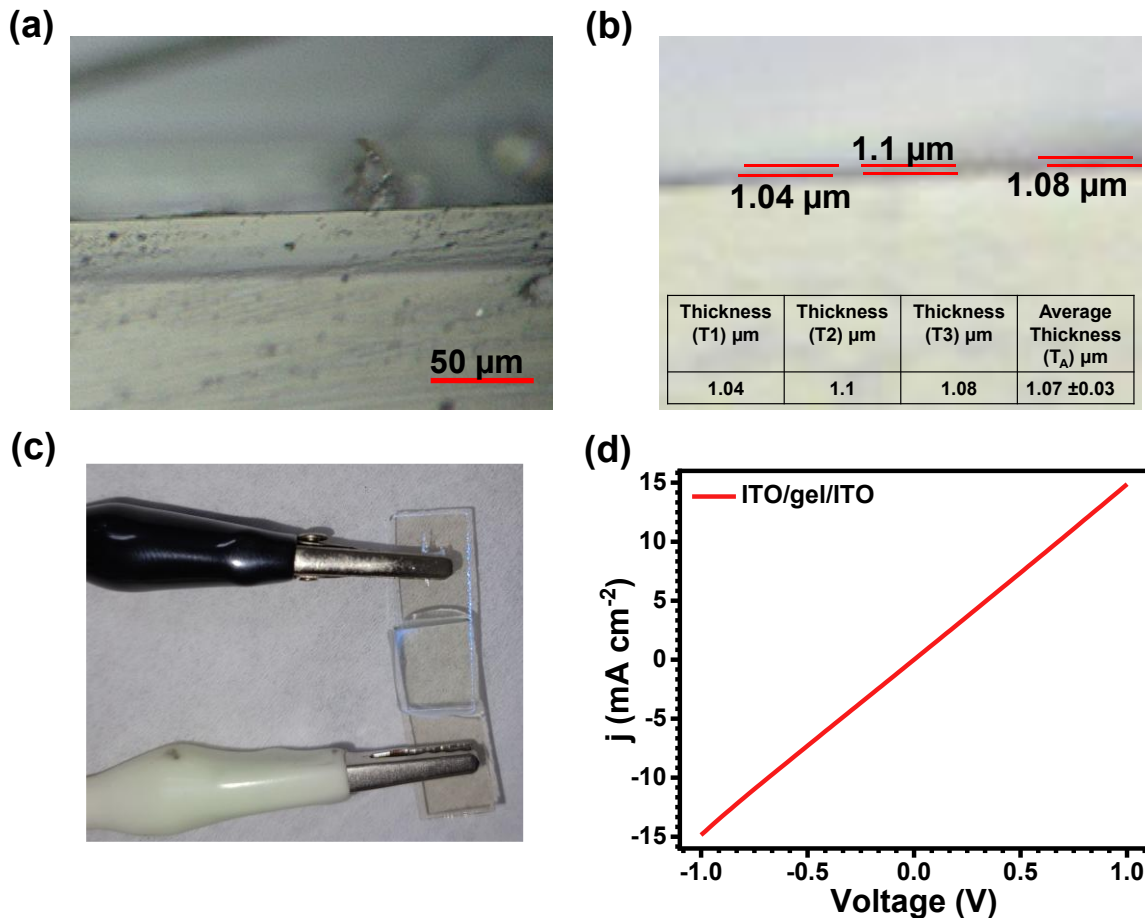


Fig S14. optical microscopy image and j-V behavior of the device configuration ITO/gel/ITO, which was used as a reference in our DC-based electrical measurement. (a) Cross-sectional optical microscopy image, (b) thickness measurement from Cross-sectional image, (c) digital image of the device used in the electrical measurement and (d) Current density(j) vs. voltage behavior of the device in the potential range -1 to +1 V. A table show the average thickness of the gel.

15. Schematic diagram and current-voltage behavior of the electrical devices

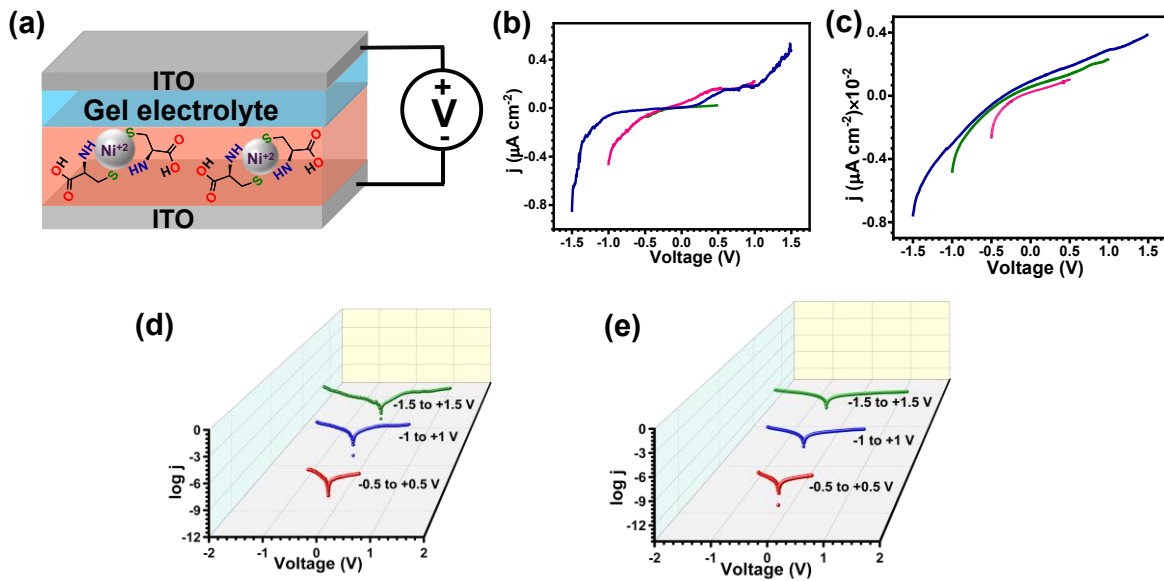


Fig S15. Device configuration and j-V characteristics of L/D-Cys-Ni (II). (a) Schematic representation of the fabricated device by chiral materials, current density vs voltage plots of (b) L-Cys-Ni (II), and (c) D-Cys-Ni (II). Semi-logarithmic plot of current density vs. voltage of (d) L-Cys-Ni (II), and (e) D-Cys-Ni (II).

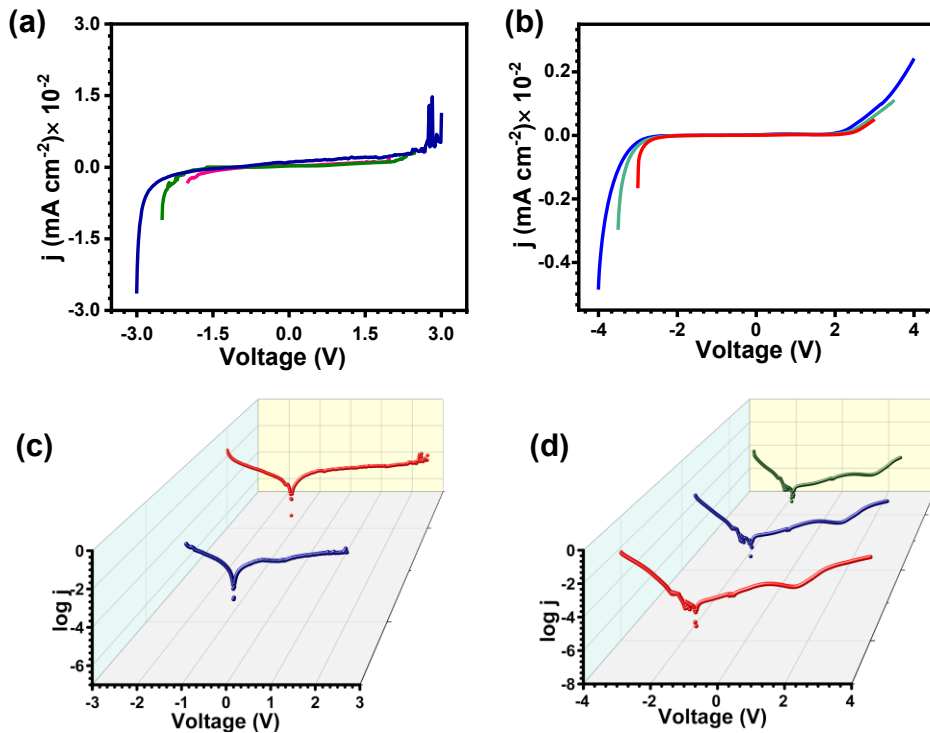


Fig S16. Current density vs. voltage (j -V) plots at extended potential windows for (a) L-Cys-Ni (II) and (b) D-Cys-Ni (II). The semi-logarithmic plot of current density vs. voltage ($\log j$ -V) at extended potential windows for (c) L-Cys-Ni (II), and (d) D-Cys-Ni (II).

16. Current density-voltage (j-V) characteristics with configuration Ni/Gel/ITO

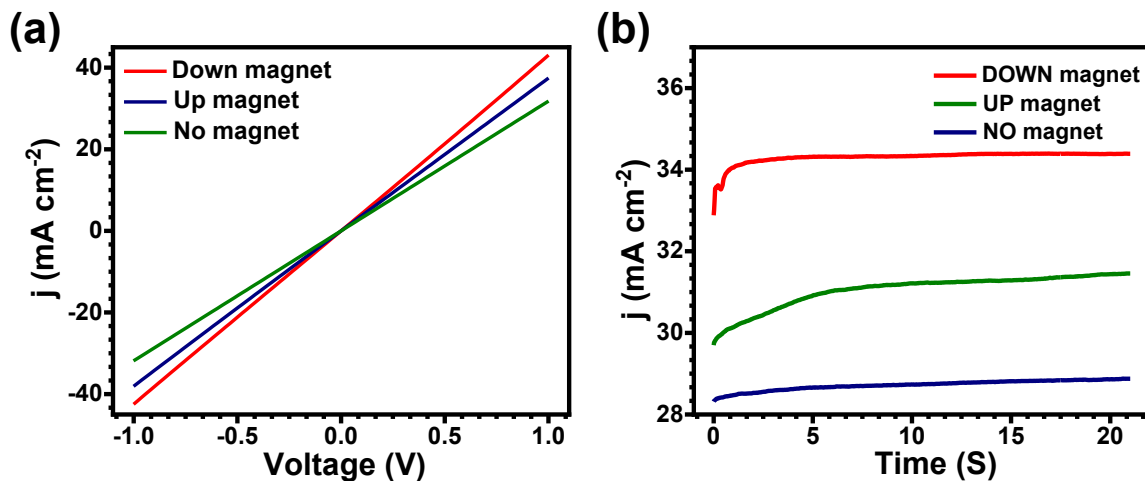


Fig S17. Current density-voltage (j -V) behavior of the device fabricated using Ni as bottom and Gel coated ITO as top electrodes. (a) j -V plot within the potential range of -1 to +1 V, (b) Current density-time (j -t) characteristic. This Ni/Gel/ITO device was used as a reference for DC-based electrical measurements.

17. Optical microscopy images

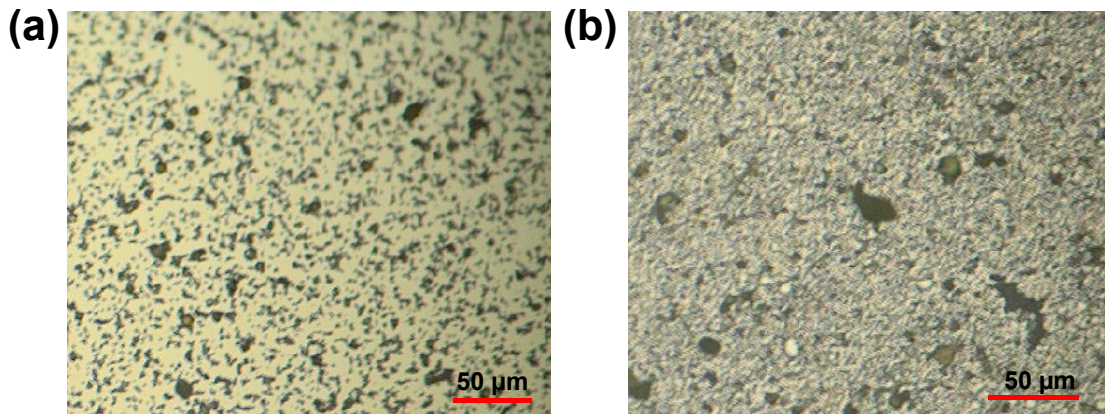


Fig S18. Optical microscopy image of Ni electrode modified with drop-casting of (a) L-Cys-Ni (II), and (b) D-Cys-Ni (II) heterostructures. Scale bars are provided in the respective images.

18. Study of film morphology without and with magnetic field

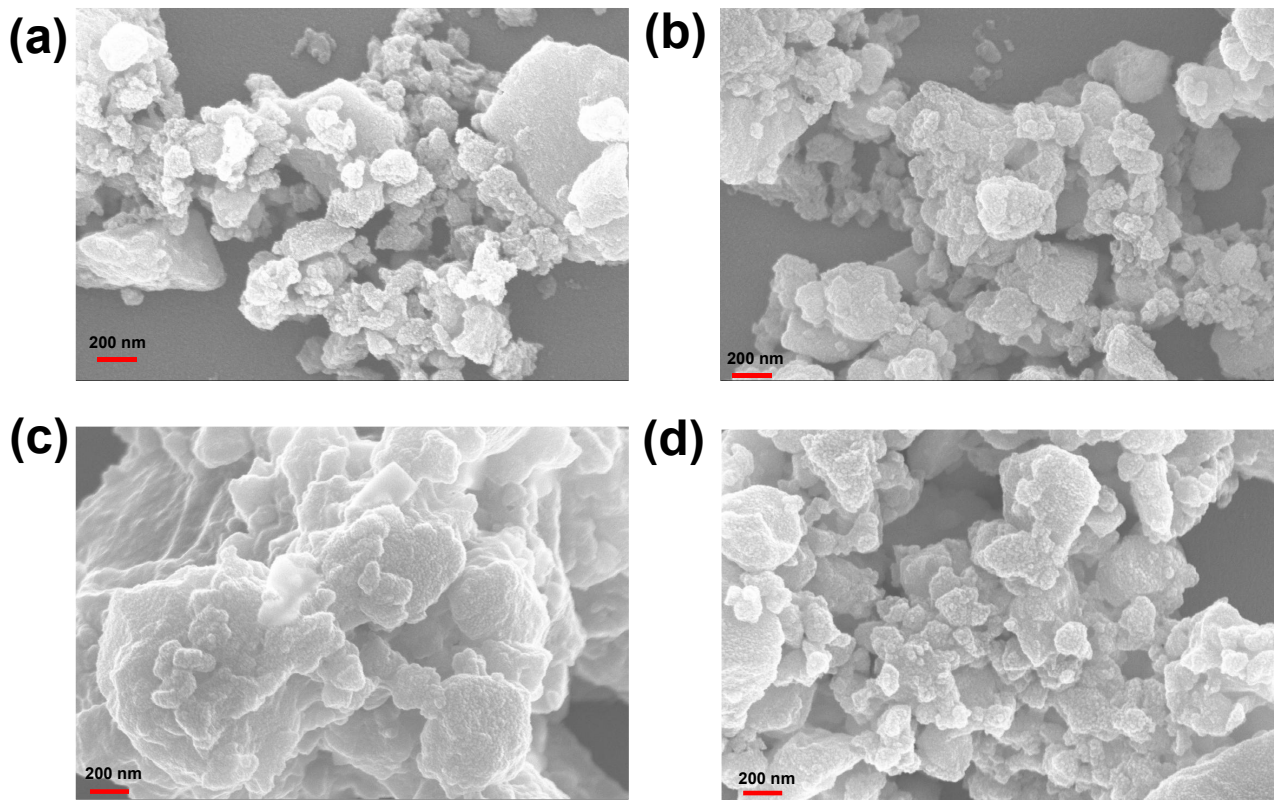


Fig S19. FE-SEM images of drop-casted materials on Ni electrode without and with magnetic field to study the effect on the surface. (a) L-Cys-Ni (II), and (b) D-Cys-Ni (II) heterostructures without magnet, (c) L-Cys-Ni (II), and (d) D-Cys-Ni (II) heterostructures with magnet. Scale bars are provided in the respective images.

19. Current density-voltage (j-V) characteristics

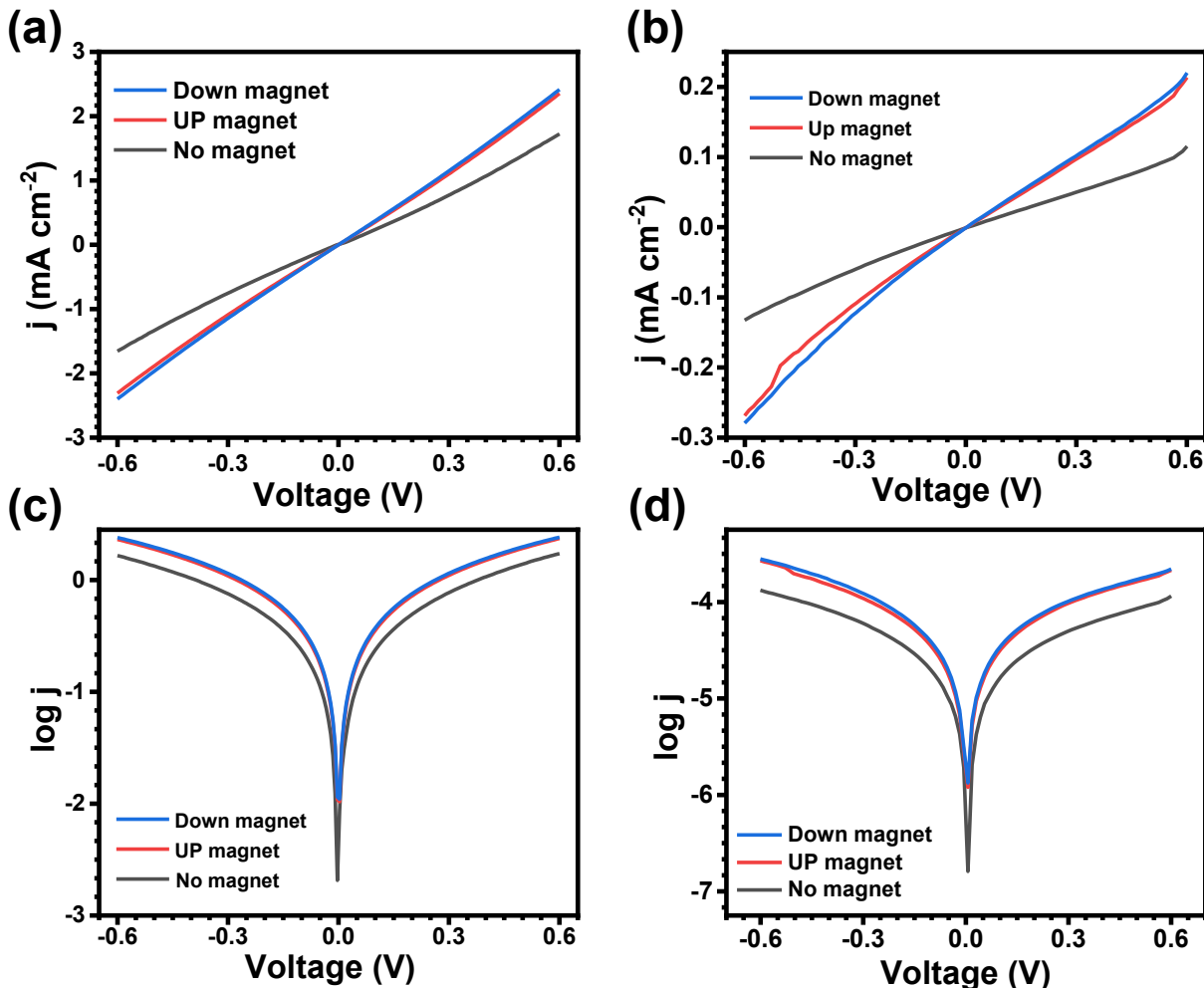


Fig S20. Current density-voltage (j-V) behavior of the synthesized chiral heterostructures with device configuration Ni/L-Cys (II)//Gel/ITO and Ni/D-Cys (II)//Gel/ITO within the applied bias -0.6 V to 0.6 V. j-V plots of (a) L-Cys-Ni (II) and (b) D-Cys-Ni (II). Semi-logarithmic plot of current density vs. voltage (log j-V) for (c) L-Cys-Ni (II), and (d) D-Cys-Ni (II).

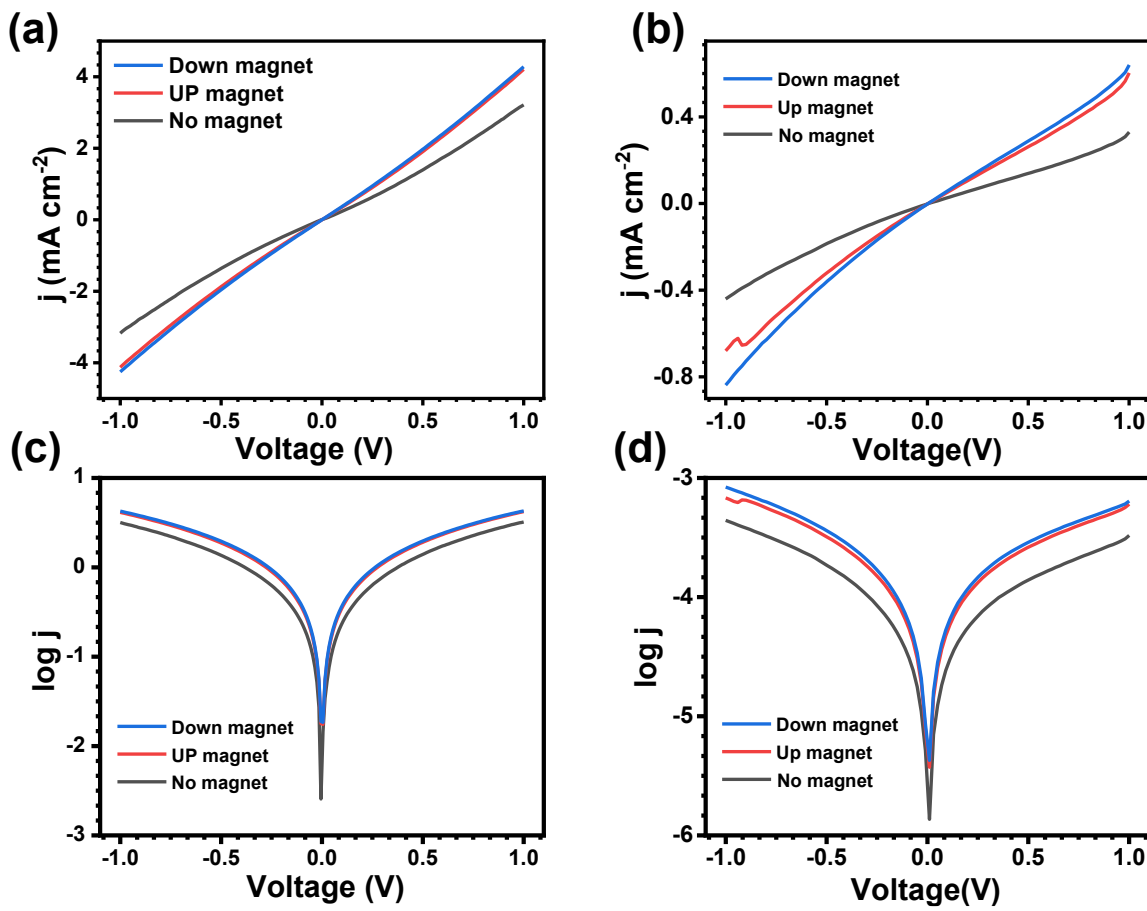


Fig S21. Current density-voltage (j -V) behavior of the synthesized chiral heterostructures with device configuration Ni/L-Cys-Ni (II)//Gel/ITO and Ni/D-Cys-Ni (II)//Gel/ITO within the applied bias ± 1 V. j-V plots of (a) L-Cys-Ni (II) and (b) D-Cys-Ni (II). The semi-logarithmic plot of current density vs. voltage of (c) L-Cys-Ni (II), and (d) D-Cys-Ni (II).

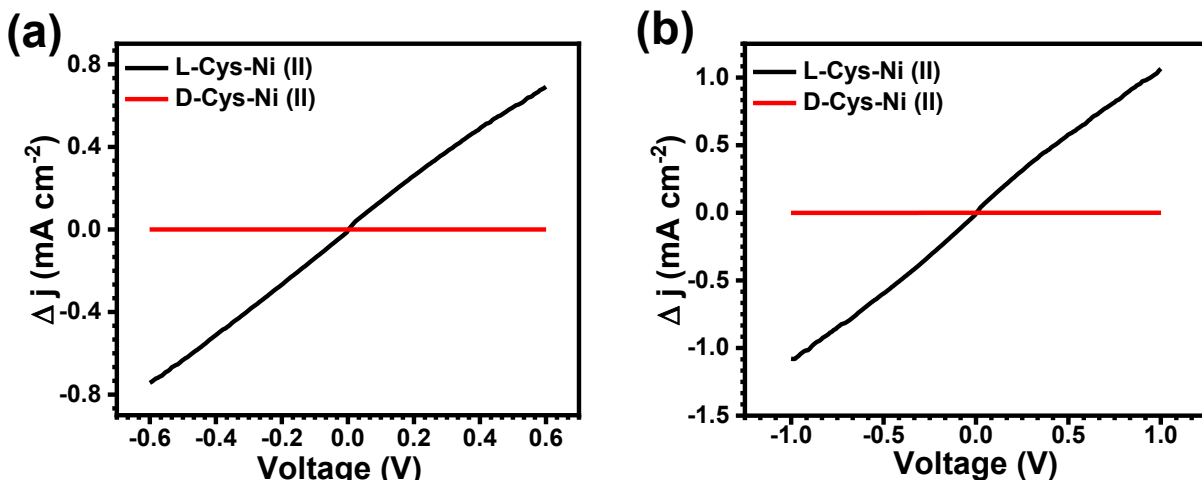


Fig S22. Comparison of current enhancement (Δj) vs. voltage plot for Ni/L-Cys-Ni (II)//Gel/ITO (black) and Ni/D-Cys-Ni (II)//Gel/ITO (red) in the presence of magnetic field for the potential window (a) -0.6 to +0.6 V, and (b) -1.0 to +1.0 V.

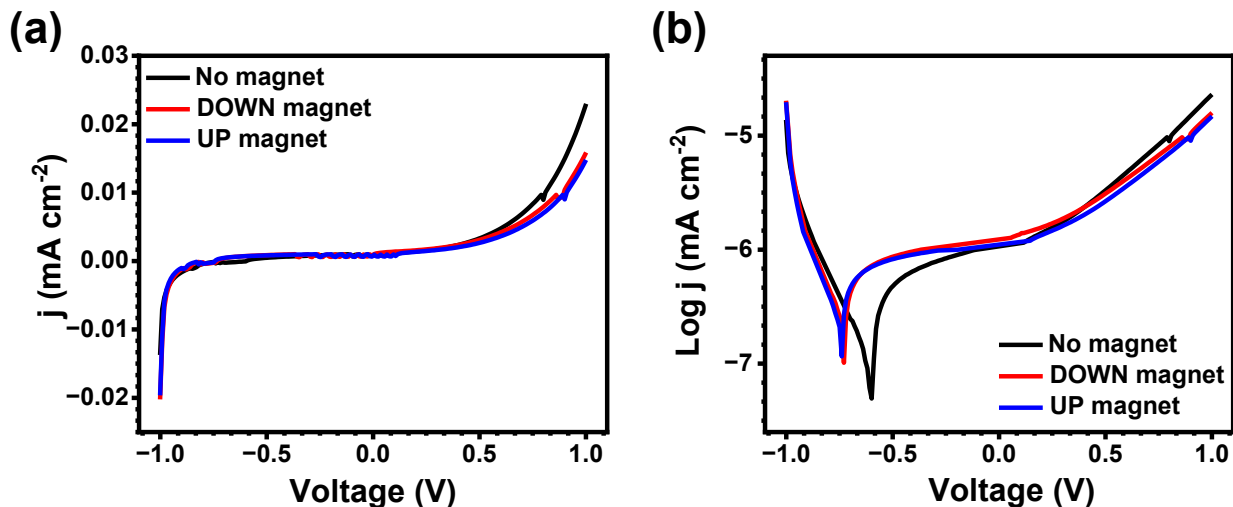


Fig S23. Current density-voltage (j -V) behavior of the synthesized achiral heterostructures with device configuration Ni/3-MPA-Ni//Gel/ITO. (a) j -V plot without and with presence of magnetic field for the potential window ± 1.0 V, and (c) The semi-logarithmic plot of current density vs. voltage of device configuration Ni/3-MPA-Ni//Gel/ITO in the bias range ± 1.0 V.

20. Solid-state device's electrical parameters

Table S3. Current density (j) values and enhancement in current density (Δj) in the presence of magnetic field for Ni/L-Cys-Ni (II)//gel/ITO and Ni/D-Cys-Ni (II)//gel/ITO at different biases of +0.6 V, +0.8 V, and +1.0 V.

| Applied Bias | L-Cys-Ni (II) (without magnetic field) j (mA cm $^{-2}$) | L-Cys-Ni (II) (with magnetic field) j (mA cm $^{-2}$) | D-Cys-Ni (II) (without magnetic field) j (mA cm $^{-2}$) | D-Cys-Ni (II) (with magnetic field) j (mA cm $^{-2}$) | Δj (L-Cys-Ni(II)) (mA cm $^{-2}$) | Δj (D-Cys-Ni(II)) (mA cm $^{-2}$) |
|--------------|---|--|---|--|---|---|
| +0.6 V | 1.723 | 2.414 | 0.115 | 0.220 | 0.691 | 0.105 |
| +0.8 V | 2.258 | 3.347 | 0.309 | 0.456 | 1.08 | 0.147 |
| +1 V | 3.21 | 4.28 | 0.33 | 0.64 | 1.07 | 0.31 |

21. Control studies for magneto electrochemical measurements

21a. Open circuit potential and magneto electrochemical measurements

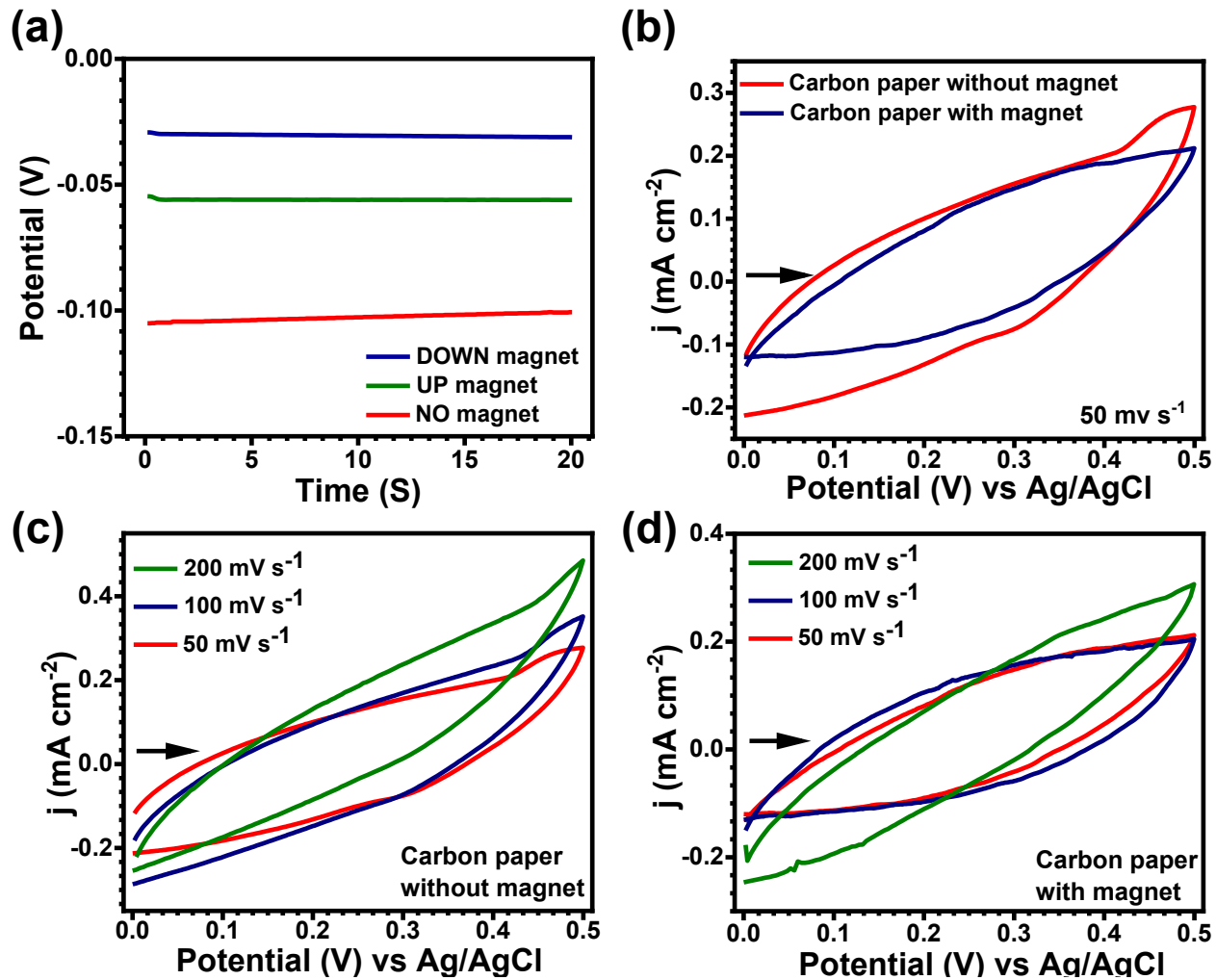


Fig S24. Magneto electrochemistry behavior of blank carbon paper. (a) measurement of open circuit potential (OCP) without and with magnetic field, (b) Comparison cyclic voltammetry of blank carbon paper with and without magnetic field at 50 mV s^{-1} . Scan rate-dependent cyclic voltammetry of bare carbon paper for (c) without magnet, and (d) with magnet condition.

21b. Scan rate-dependent magneto electrochemistry of carbon paper working electrode

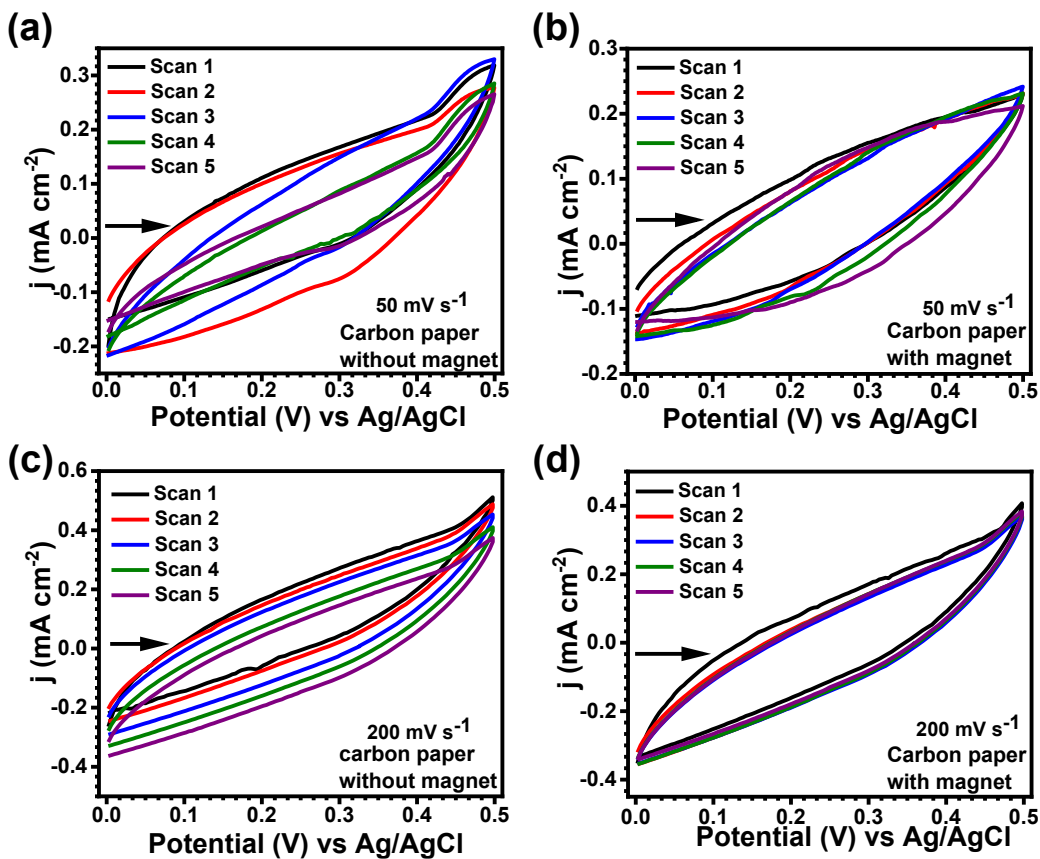


Fig S25. Scan rate-dependent magneto electrochemistry of carbon working electrode. Cyclic voltammogram at 50 mV s^{-1} for (a) without and (b) with magnet condition. Cyclic voltammogram at 200 mV s^{-1} for without and (b) with magnet condition.

22. Statistical data on magneto-electrochemistry measurements

Table S4. Characteristic change in oxidation, reduction potential, and enhancement in current density (j) in the presence of magnetic field

| Sample | oxidation potential /increase in j | reduction potential/increase in j (%) |
|-----------------|--------------------------------------|---|
| L-Cys-Ni (II) 1 | 0.373 V to 0.361 V / 58% | 0.284 V to 0.266 V/ 83% |
| D-Cys-Ni (II) 1 | 0.385 to 0.380 V / 15% | 0.272 to 0.262 V / 48% |
| L-Cys-Ni (II) 2 | 0.35 V to 0.36 V / 15% | 0.29 V to 0.284 V / 73% |
| D-Cys-Ni (II) 2 | 0.375 V to 0.386 V/ 89% | 0.25 V to 0.27 V / 72% |

23. Magneto-electrochemistry of achiral Ni (II) heterostructures, and Ni(OH)₂

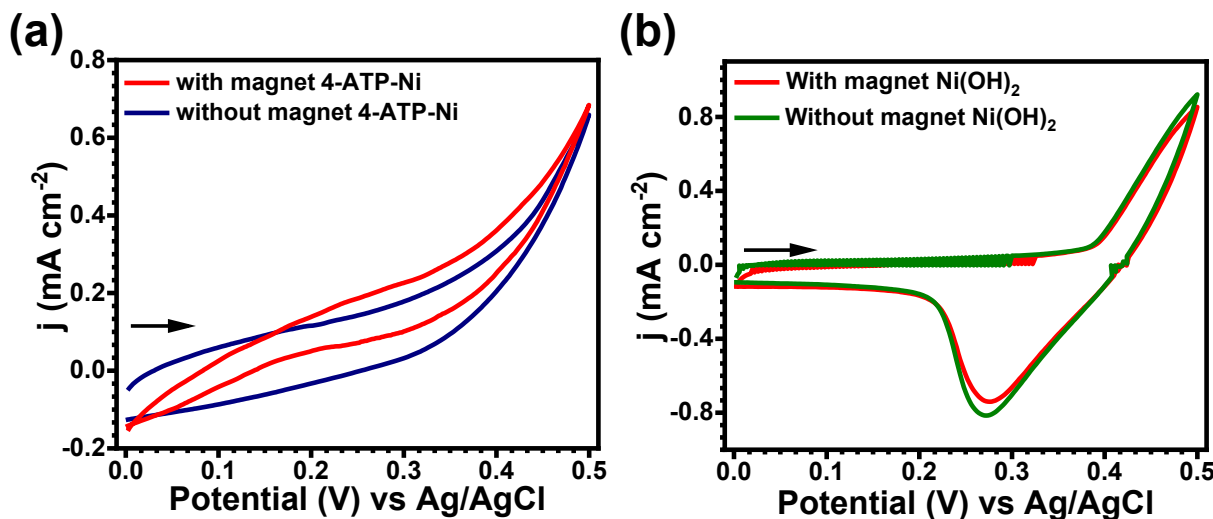


Fig S26. CVs of (a) 4-amino thiophenol-Ni modified carbon paper with and without magnetic field, (b) $\text{Ni}^{+2}/\text{Ni}^{+3}$ redox behavior in Ni(OH)_2 without and with magnetic field.

24. Chronoamperometry measurements for Chiral L/D-Cys-Ni (II)

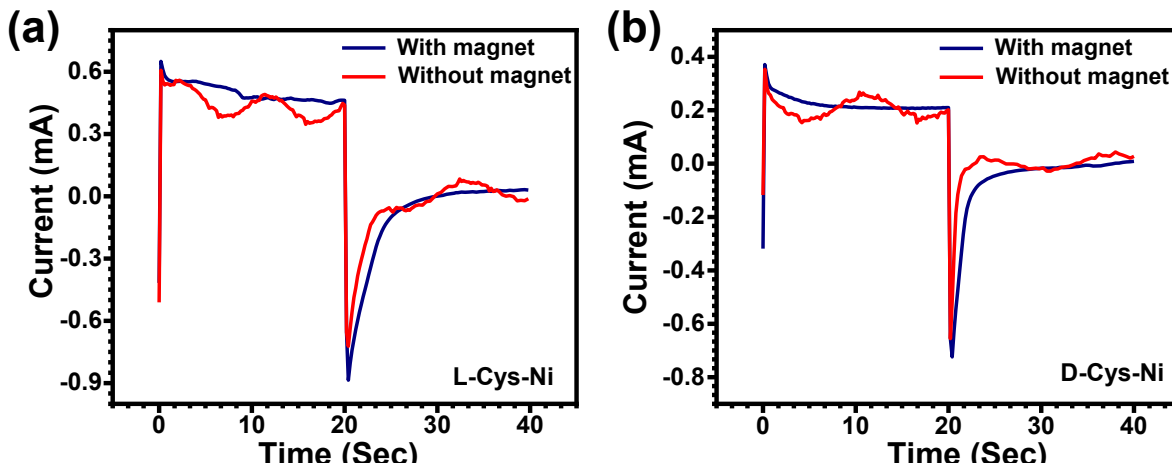


Fig S27. Current vs. time (i - t) behavior of (a) L-Cys-Ni (II), (b) and D-Cys-Ni (II), without and with an external magnetic field.

25. Electrochemical parameters deduced from the equivalent model circuit

Table S5. Table for equivalent circuit elements values of fitted electrochemical impedance spectra (EIS).

| Circuit Elements | L-Cys-Ni (II) | L-Cys-Ni (II) in a magnetic field | D-Cys-Ni (II) | D-Cys-Ni (II) in magnetic field |
|---------------------------|---------------|-----------------------------------|---------------|---------------------------------|
| $R_{\text{cntc}}(\Omega)$ | 5.51 | 5.68 | 3.08 | 5.47 |
| $R_{\text{ct}}(\Omega)$ | 541 | 216 | 108 | 5.17 |

| $C_{dl}(F)$ | 61.6 μ | 1 | 78.4 μ | 63 μ |
|--|---------------|---------------|---------------|--------------|
| CPE₁(mFs^(a-1)) Exponent (n) | 1.41 0.051 | 3.76 0.533 | 1.53 0.559 | 107 0.938 |
| CPE₂(mFs^(a-1)) Exponent (n) | 2.26 0.523 | 4.76 0.5 | 1.03 0.25 | 4.11 0.5 |

26. References

- 1 A. Ganguly, S. Sharma, P. Papakonstantinou and J. Hamilton, *J. Phys. Chem. C*, 2011, **115**, 17009–17019.
- 2 B. Sivaranjini, R. Mangaiyarkarasi, V. Ganesh and S. Umadevi, *Sci. Rep.*, 2018, **8**, 1–13.
- 3 Z. H. Sheng, L. Shao, J. J. Chen, W. J. Bao, F. Bin Wang and X. H. Xia, *ACS Nano*, 2011, **5**, 4350–4358.
- 4 Y. Tokudome, A. Koyama, H. Murata, K. Okada, A. Nakahira, S. Nishimura and M. Takahashi, *J. Sol-Gel Sci. Technol.*, 2022, **104**, 580–587.